Microstructure and Texture Evolution during Single- and Multiple-Pass Friction Stir Processing of Heat-Treatable Aluminum Alloy 2024

NARESH NADAMMAL, SATISH V. KAILAS, JERZY SZPUNAR, and SATYAM SUWAS

Microstructure and crystallographic texture evolution during single- and multiple-pass friction stir processing (FSP) of an age-hardenable aluminum alloy 2024 (Al-Cu-Mg) was investigated. Multiple-pass experiments were carried out using two different processing strategies, multi-pass FSP, and multi-track FSP. Effect of a post-FSP heat treatment above and below the solutionizing temperature of the alloy was also studied. FSP experiments were carried out using an optimal set of parameters. Characterization tools used in the study include scanning electron microscopy (SEM), electron back-scattered diffraction (EBSD), electron probe micro-analyser (EPMA), and X-ray diffraction (XRD). Microstructural features indicate the occurrence of particle stimulated nucleation (PSN) assisted dynamic recrystallization (DRX) as the dominant microstructural evolution mechanism in the nugget zone. Geometrical coalescence occurred, leading to the formation of some larger grains in the nugget zone. Heterogenous micro-texture distribution was observed in the nugget zone with the bulk textures consisting of FCC shear texture components dominated by A_1^*/A_2^* and C. Microstructure and texture in the nugget zone remained stable after both routes of multiple-pass processing, demonstrating the possibility of FSP to produce bulk volume of fine-grained materials. Post-FSP heat treatment indicated the stability of microstructure and texture up to 723 K (450 °C) owing to relatively lower strain energies retained after FSP.

I. INTRODUCTION

ALUMINUM alloys are widely used in aerospace and ground transport applications due to their high strength-to-weight ratio and good corrosion resistance. Heat-treatable aluminum alloys have the highest specific strength among all the alloys due to the strengthening obtained through precipitation hardening. Highest strength among all the heat-treatable alloys is exhibited by 7XXX (Al-Zn-Mg-Cu) series, and the same is preferred when strength is the overriding criterion.[1] In situations when damage tolerance[2] is a primary requirement, 2XXX series (Al-Cu and Al-Cu-Mg) is widely used. In the 2XXX series of aluminum alloys, the alloy 2024 and its advanced versions are the most commonly used structural materials for manufacturing critical components such as fuselage skins of aircrafts. The addition of Mg into the Al-Cu system leads to a faster and significantly different precipitation and recrystallization kinetics in the alloy 2024, compared to the conventional Al-Cu alloys.[3]

To further enhance the strength of these alloys grain refinement is a possibility. Severe Plastic Deformation (SPD) techniques,[4–7] which are based on the top-down approaches in materials processing technology, offer ample scope for grain refinement, and property enhancement in structural materials. The most significant SPD techniques include equal channel angular processing (ECAP), High-pressure Torsion (HPT) and Accumulative Roll Bonding (ARB).[8–15] FSP was introduced as a SPD technique in the year 2000 by Mishra et al.[16]; FSP technique was derived from the revolutionary solid state joining method of friction stir welding (FSW). With the advantage of using a conventional milling machine for processing, FSP has become one of the most promising methods for bulk materials processing. Unlike the processes that are discontinuous in nature such as

NARESH NADAMMAL and SATISH V. KAILAS are with the Department of Mechanical Engineering, Indian Institute of Science, Bangalore, Karnataka, 560012, India. Contact e-mail: nareshnn@mecheng.iisc.ernet.in JERZY SZPUNAR is with the Department of Mechanical Engineering, University of Saskatchewan, Saskatoon, SK S7N 5A9, Canada. SATYAM SUWAS is with the Department of Materials Engineering, Indian Institute of Science, Bangalore, Karnataka, 560012, India.

ECAP, FSP is a continuous process where fine-grained microstructures can be produced. Further, fine-grained structures can be generated in a local region or throughout the complete plate. During the process, high temperatures, close to $0.7T_m$, get generated, which can lead to a relatively larger grain size. However, with many advantages such as simplicity of the processing, eco-friendliness, and the ease of scaling up for bulk production, this technique unveils a huge potential as an industrial process.

Major parameters that control the efficiency of FSP include tool rotational speed, tool traverse speed, tool tilt angle, and tool geometry. For a single-pass FSP, a bottom-up approach developed by the present authors[17] has been used in optimizing the process parameters. FSP has been perceived as a grain refinement technique, and hence, the most interesting region in the processed materials is the nugget zone (NZ). It is also possible that in a process such as FSP, where the continuous stirring of work piece is caused by the high rotation speed of the tool pin, observation from a single location in the NZ cannot represent the path taken by the material during the microstructural evolution that has occurred in the complete NZ. Hence, it is important to characterize different locations in the NZ to get a better idea about the mechanisms involved in the microstructural evolution and the crystallographic texture development.

Microstructural studies on AA 2024-T3 friction stir welds were carried out by Sutton et al.[18] It was observed from their study that FSW process creates a segregated banded microstructure consisting of alternating hard particle-rich and hard particle-deficit regions in the NZ. Fracture experiments on the same material revealed that the banded microstructure influences the macroscopic fracture process in the welded material through the crack path tending to follow the particle-rich regions in the microstructure. In another study by Charit et al.,[19] high strain rate superplasticity was achieved on AA 2024-T4 after FSP. Ductility of the processed material was significantly higher than that of the starting material at a comparable temperature and strain rate range. Superplasticity was achieved at higher strain rates of 10^{-2} to 10^{-1} s^{-1} in the same material. The maximum elongation of 525 pct could be achieved at 703 K (430 °C) and a strain rate of 10^{-2} s^{-1} in the alloy 2024. The strain rate sensitivity exponent 'm' (~ 0.5) in their study indicated grain boundary sliding (GBS) as the dominant deformation mechanism. Superplastic properties deteriorated at or above 743 K (470 °C) owing to abnormal grain growth.

Aydin et al.[20] investigated FSW of the alloy 2024 with the starting materials in different tempered conditions and its tensile properties were compared. The heat-treated states displayed different fracture locations during tensile testing. The fracture of 2024-O joint occurred in the un-processed region of the starting material. For the weld prepared from an initial temper of 2024-W, fracture location was at or near the NZ on the advancing side (AS). In 2024-T4 and 2024-T6 joints, the fracture occurred near or at the interface between the NZ and the thermo-mechanically affected zone (TMAZ) on the AS. It was concluded from their work that as the driving force for the precipitation of the starting material was increased (based on temper), fracture location of the weld joints approached the NZ.

As a technique to produce fine-grained materials, it is anticipated that single-pass FSP might not suffice the requirement of bulk grain refinement. In such a situation, multiple-pass processing could be more useful. Multiple-pass processing can be carried out in two different ways; (1) by overlapping passes in the same region, termed as Multi-Pass FSP (MP-FSP) and (2) through parallel passes for bulk production of fine-grained materials, termed as Multi-Track FSP (MT-FSP). In MP-FSP, the processed material undergoes further plastic deformation and exposure to high temperature as in the previous pass. In case of fine-grained microstructures, microstructural stability is an important issue that needs to be addressed while considering the application of processed materials at elevated temperatures. Along with the microstructural stability, the other important factor is the variation in bulk crystallographic texture during multiple-pass processing. Few attempts[21] have been made to study the stability of grain size during multiple-pass FSP. However, information regarding texture evolution in multiple-pass FSP, to the best of our knowledge, is not available in the existing literature. Crystallographic texture will have a strong influence on the mechanical properties of the processed materials.

The objective of the present study is to develop a comprehensive understanding on the evolution of microstructure and texture during FSP of an age-hardenable aluminum alloy 2024. To broaden the existing knowledge on FSP of aluminum alloys, the microstructural and textural stability of the processed materials has been investigated during multiple-pass FSP and after a post-FSP heat treatment at two different temperatures.

II. EXPERIMENTAL DETAILS

A. Material

The material selected for the present study is aluminum alloy 2024, which is a heat-treatable alloy with Cu and Mg as the major alloying elements. The starting material for the present investigation was obtained from PMC Corporation, Bangalore, as a 6-mm-thick plate in the T3 temper, which is solution heat treated, cold worked, and then naturally aged. Elemental composition of the as-received alloy was verified using an EPMA and is presented in Table I. The elemental composition of precipitate particles having size larger than 0.5 μm was also calculated using EPMA and the results are given in Figure 3.

B. Processing

The tool was made from the material hot die steel (HDS) in H13 hardened condition. Tool shoulder diameter was 26 mm, which was tapered from a 28-mm cylinder with the tool pin shape of a frustum of a cone having top diameter of 6 mm and a bottom

Table I. Elemental Composition of the Alloy 2024 in Weight Pct

Element	Al	Cu	Mg	Mn	Si	Zn
Weight Pct	94.8	3.64	1.45	0.45	0.06	0.05

diameter of 4 mm. Flat shoulder geometry was considered with the tool tilt angle kept constant at 2 deg. A tool pin length of 5.4 mm with a right-handed thread having a pitch of 1.5 mm was used. The threaded tool pin was selected to have a better material mixing during processing, especially when the material flows in the vertical direction. The bottom-up approach developed by the present authors was used for obtaining the optimal process parameters.[17] Same parameters were used in the present study, and the FSP experiments were carried out perpendicular to the rolling direction in the plate. The optimal process parameters are as follows: tool shoulder plunge depth of 0.23 mm into the work piece, tool rotation rate of 350 RPM, and a tool traverse speed of 95 mm/min.

Multiple-pass FSP was carried out in two different ways, MP-FSP and MT-FSP, with successive passes carried out at shorter processing distances. In this way, the effect of successive pass (or passes) on the previous pass (or passes) could be studied. In MP-FSP, 100 pct overlap was allowed between the consecutive passes. Four passes were processed in this way, and the resulting samples were designated as MP-1, MP-12, MP-123, and MP-1234 corresponding to the first, second, third, and fourth pass respectively in the same region. In MT-FSP, an overlap ratio (OR) of 0.33 was maintained between the successive passes. Overlap ratio is defined as $OR = 1 - (L/R)$, where L is the centre-to-centre distance between successive passes and 'R' is the top diameter of tool pin. In this study 'L' was taken as 4 mm and 'R' as 6 mm leading to the overlap ratio 0.33, rendering partial penetration between the nugget zones of successive passes. Successive tracks were processed in the advancing side of the previous pass. This is to avoid the sharp boundary, which is usually observed in the advancing side of the friction stir welded/processed materials. Such a boundary in the processed region could act as a region of stress concentration during tensile or fatigue testing. In the present investigation, four parallel tracks were processed and the sample designation system followed was MT-1, MT-12, MT-123, and MT-1234, which correspond to the first, second, third, and fourth parallel track, respectively. Tracking the nugget zone of the first pass is possible with MT-FSP and the sample designation system adopted for this was 1-1, 12-1, 123-1, and 1234-1.

C. Metallography and Characterization

Transverse sections of the optimal and multiple-pass processed samples were polished for the detailed microstructural characterization. Processed samples were cut using a band-saw, which led to a very rough cross-section. These samples were further polished on a belt grinder using an emery paper of grit size 80, which caused the removal of roughness. Further polishing was carried out using SiC papers of grit sizes P220, P400, P600, P800, and P1000. This was followed by cloth polishing using SiC powder corresponding to grit size of P1200 and water as a lubricant. Fine polishing was carried out using diamond suspension with particle sizes of 3 and 1 μm. Fine polished samples were etched using Keller's reagent (95 mL distilled water, 2.5 mL HNO3, 1.5 mL HCl and 1 mL HF) for Optical Microscopy (OM) characterization. Macrograph of the processed zone was captured using a low-magnification Metallovert optical microscope.

For electron microscopy, fine polished samples were electro-polished in a Struer's Lectropol-5 electro-polisher using the standard A2 electrolyte. Electrolyte was refrigerated at about 268 K to 275 K (-5 °C to 2 °C) few minutes prior to the electro-polishing. Electro-polishing was carried out at 26 V for 20–25 seconds. SEM imaging was carried out on an ESEM Quanta microscope (FEI Company, Quanta 200). EBSD attachment to the SEM was utilized for obtaining the simultaneous information on microstructure and micro-texture. During EBSD analyses, specimens were kept inside the SEM chamber in an identical manner to match with the frame of reference for simple shear deformation.[22] EBSD scans were recorded at the exact centre line of the nugget zone and across the thickness, so that the threaded tapered geometry of the tool pin did not cause any difficulty in identifying the texture components. TSL orientation imaging microscopy (OIM) software was used for the EBSD data analysis. For the micro-texture analysis of EBSD data, a partition was given to include only scan points having a minimum confidence index (CI) of 0.1.

Bulk texture was measured in the transverse section of the processed samples using a Bruker D8-Discover goniometer attached with the area detector Vantec-500. During bulk texture measurement of the multi-pass FSP samples, the centre of nugget zone was focussed using the laser arrangement attached to the goniometer; this was done to avoid any diffraction from the other regions such as the TMAZ and heat-affected zone (HAZ).

As a further study on the stability of FSP microstructures and understanding the dominance of static/dynamic restoration mechanisms during FSP, optimally processed samples were heat treated at temperatures above and below the solutionizing temperature for this alloy. Solutionizing temperature for this alloy is around 773 K (500 °C),[3,20] and hence, the samples were heated at 723 K and 823 K (450 °C and 550 °C) for 30 minutes, in a furnace having an allowable temperature tolerance of ±6 K. Characterization of the post-FSP heat-treated samples were also carried out using EBSD.
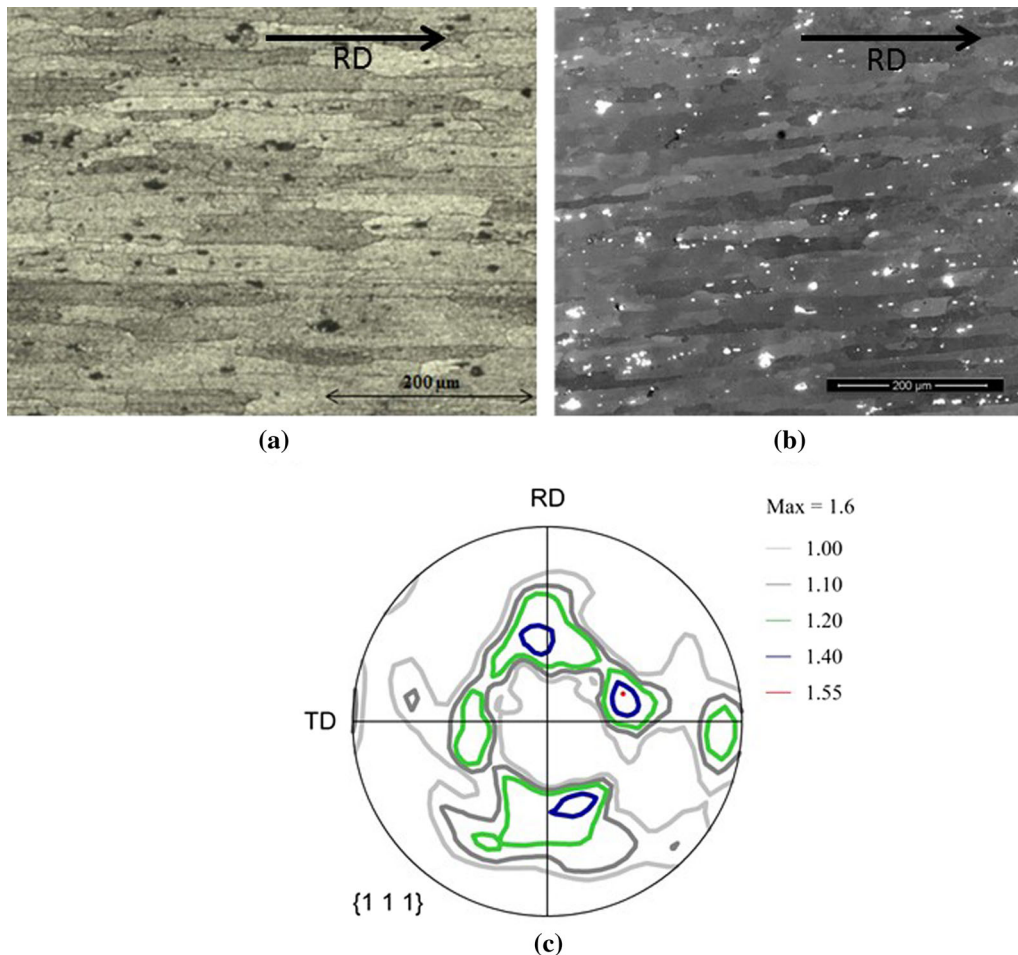
Fig. 1—Microstructure of the starting material of alloy 2024 (*a*) optical micrograph (*b*) back-scattered electron micrograph (*c*) bulk texture in the starting material represented using a 111-pole figure, RD-Rolling Direction.

III. RESULTS AND DISCUSSION

A. *Microstructure and Texture Evolution During Single-Pass FSP*

Microstructure of the starting material obtained using the optical and scanning electron microscopy is displayed in Figures 1(a) and (b). Both micrographs reveal a typical rolled microstructure with large grains elongated in the rolling direction. The alloy is precipitation hardenable, and contains some large precipitate particles in the microstructure that are represented as dark and bright spots in the optical and back-scattered electron image respectively. Crystallographic texture of the starting material is also represented in Figure 1(c) using a 111-pole figure. The intensity of the initial texture is weak with the major components observed as cube and rotated cube.

Figure 2 depicts the microstructure evolution in the NZ using the orientation imaging microscopy (OIM) maps obtained from the recorded EBSD scans. Image quality (IQ) maps taken across the thickness at the top, middle, and bottom is given, respectively, by Figures 2(a) through (c). Figure 2(d) displays the inverse pole figure (IPF) map with the color code to

emphasize the banded microstructural feature observed as elongated grains in the bottom of nugget zone.

An equi-axed microstructure is present across the thickness with the average grain sizes of 7.6, 6.2, and 7.5 μm observed at the top, middle, and bottom of the nugget zone, respectively. Grain boundary fractions calculated based on the average length of boundaries (EBSD scan area is maintained in every scan) is given in Table II. Low-, medium-, and high-angle grain boundaries are defined as those having misorientations 3–5 deg, 5–15 deg, and greater than 15 deg, respectively.[23] The relatively lower fraction of high-angle grain boundaries is observed at the bottom of nugget zone where the density of medium-angle boundaries is also the highest. This could be due to some of the elongated grains observed in the bottom of the nugget zone. These grains are presumably stable orientation in the starting material. The effect of heat input into the bottom of nugget zone during FSP will be lesser in aluminum alloys due to their high thermal conductivity, which can also cause the heat removal at a faster rate into the backing plate. Lowest strain and strain rates are also observed in the bottom as compared to the top, and hence lesser the shear deformation.[24] Therefore, the grains that are
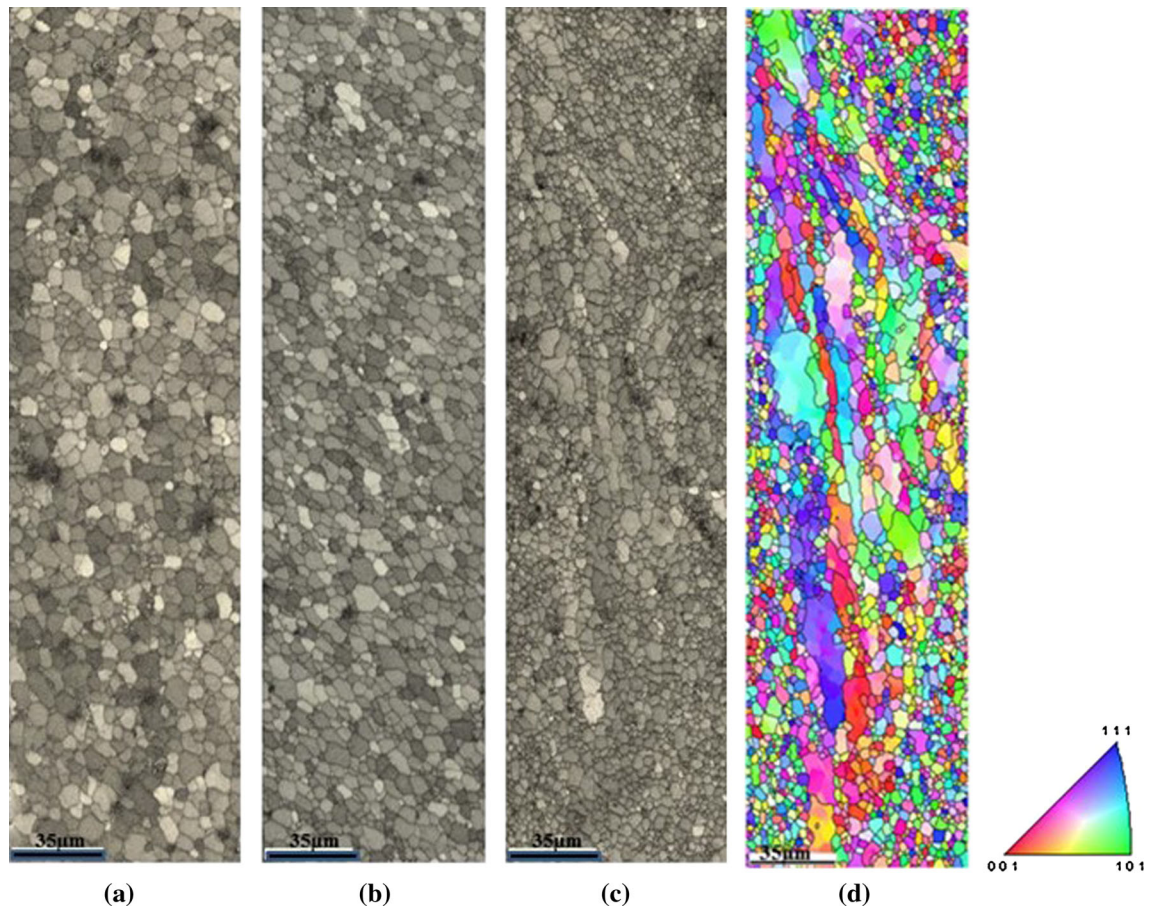
Fig. 2—OIM maps obtained from EBSD. Image quality map of the optimally processed sample representing the nugget zone microstructure at (*a*) top (*b*) middle (*c*) bottom and (*d*) IPF map corresponding to (*c*).

Table II. Number Fraction and the Types of Grain Boundary Misorientations Observed at Different Locations in the Nugget Zone of the Optimally Processed Alloy 2024

Misorientation	Number Fraction at Locations (Pct)		
	Top	Middle	Bottom
3-5 deg	15	13	10
5-15 deg	10	7	21
15-65 deg	75	80	69

already oriented in a stable configuration do not change much during the deformation induced by the tool pin. Instead, such grains are likely to fragment and increase the misorientations within it.

Microstructure observed in the nugget zone after FSP indicates the occurrence of dynamic recovery (DRV) as well as dynamic recrystallization (DRX). The back-scattered electron micrographs shown in Figure 3(a) reveal most of the precipitates at the grain boundaries. Higher magnification micrograph in Figure 3(b) highlights a large precipitate particle. The composition of the precipitate obtained through EPMA confirmed the particle as Al_2CuMg, which is the equilibrium precipitate

observed in the alloy.[25] The size of the particle is larger than 1 μm. It is possible that such a large particle has been formed through the coarsening of an existing particle as the temperatures involved in FSP are high enough for the same to occur.[26] Due to the moderate-to-high cooling rates involved, the possibility of formation of such a large particle through the dissolution and re-precipitation occurring during FSP can be excluded. Hence, during the growth of these particles, it may be possible that they can act as nuclei for recrystallization. The strain field near the boundary between the particle and matrix can create bulges of sizes large enough to grow as nuclei for grain growth.[27]
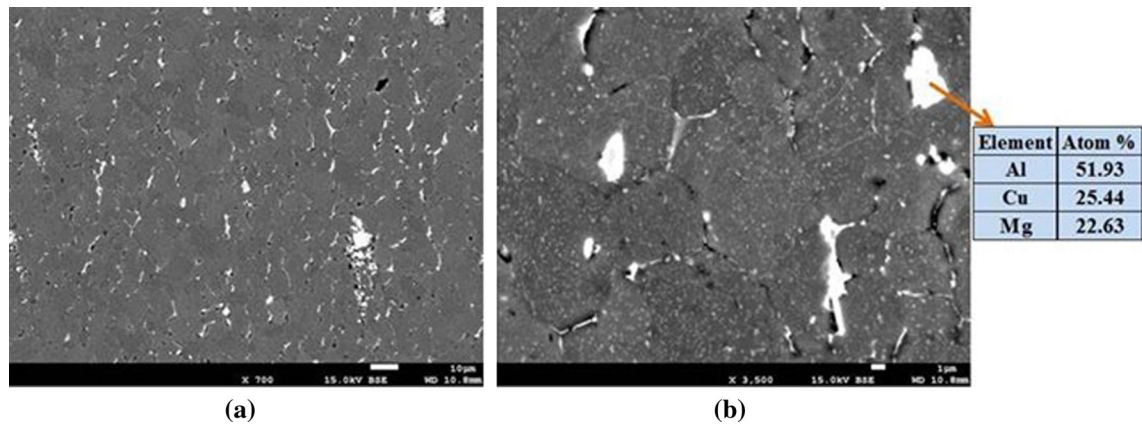
Fig. 3—Back-scattered electron micrograph representing the top of nugget zone in the optimally processed sample of the alloy 2024 (*a*) lower magnification micrograph indicating the presence and distribution of large precipitate particles especially at the grain boundaries (*b*) higher magnification micrograph with a large particle and composition of the same.
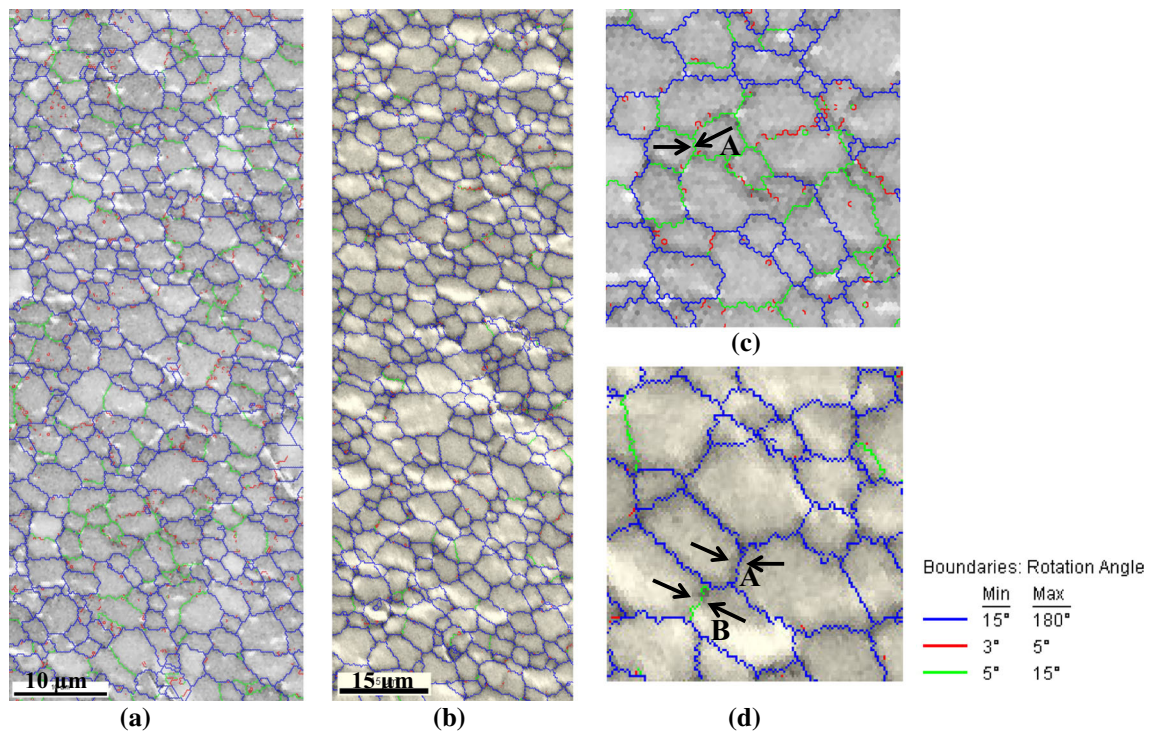

Fig. 4—EBSD generated grain boundary super-imposed IQ map representing the microstructure evolution in the nugget zone of the alloy 2024 at (*a*) bottom (*b*) middle; (*c*) and (*d*) selected regions from these IQ maps depicting the various stages of grain growth.

In such a situation, PSN can be the dominant nucleation mechanism[28] for DRX in the alloy during FSP.

PSN is the dominant micro-mechanism pertaining to the nucleation for DRX during FSP of the alloy 2024; microstructural features indicate normal grain growth in the nugget zone. Grain growth in 2-D occurs through two major mechanisms, Burke and Turnbull mechanism and geometric coalescence.[29,30] The criterion for operation of both these mechanisms is the reduction in the grain boundary curvature in a triple junction. A detailed description on the operation of these mechanisms is given in a recent paper.[31]

Table III. Ideal Components of Simple Shear Texture in FCC Materials[37]

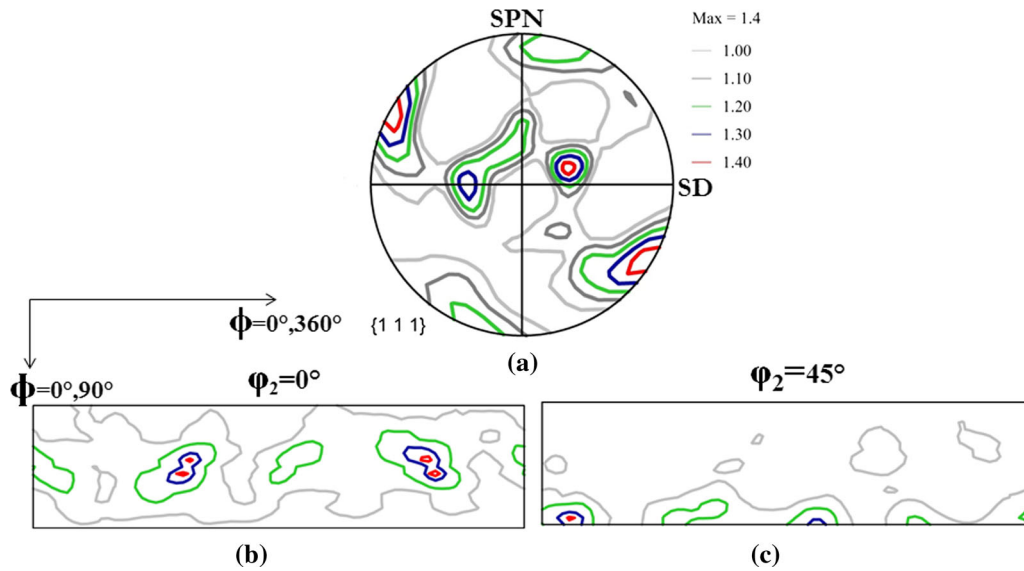| Component Designation	Miller Indices
$A_1{}^*$	$\{\bar{1}\bar{1}1\}\langle112\rangle$
$A_2{}^*$	$\{11\bar{1}\}\langle112\rangle$
A	$\{1\bar{1}\bar{1}\}\langle110\rangle$
$\bar{A}$	$\{\bar{1}11\}\langle\bar{1}\bar{1}0\rangle$
B	$\{\bar{1}12\}\langle110\rangle$
$\bar{B}$	$\{1\bar{1}\bar{2}\}\langle\bar{1}\bar{1}0\rangle$
C	$\{001\}\langle110\rangle$

Fig. 5—Bulk texture in the optimally processed sample of the alloy 2024 represented as (*a*) 111-pole figure (SPN- Shear Plane Normal and SD- Shear Direction) and ODF sections corresponding to (*b*) $\varphi_2 = 0$ deg (*c*) $\varphi_2 = 45$ deg.
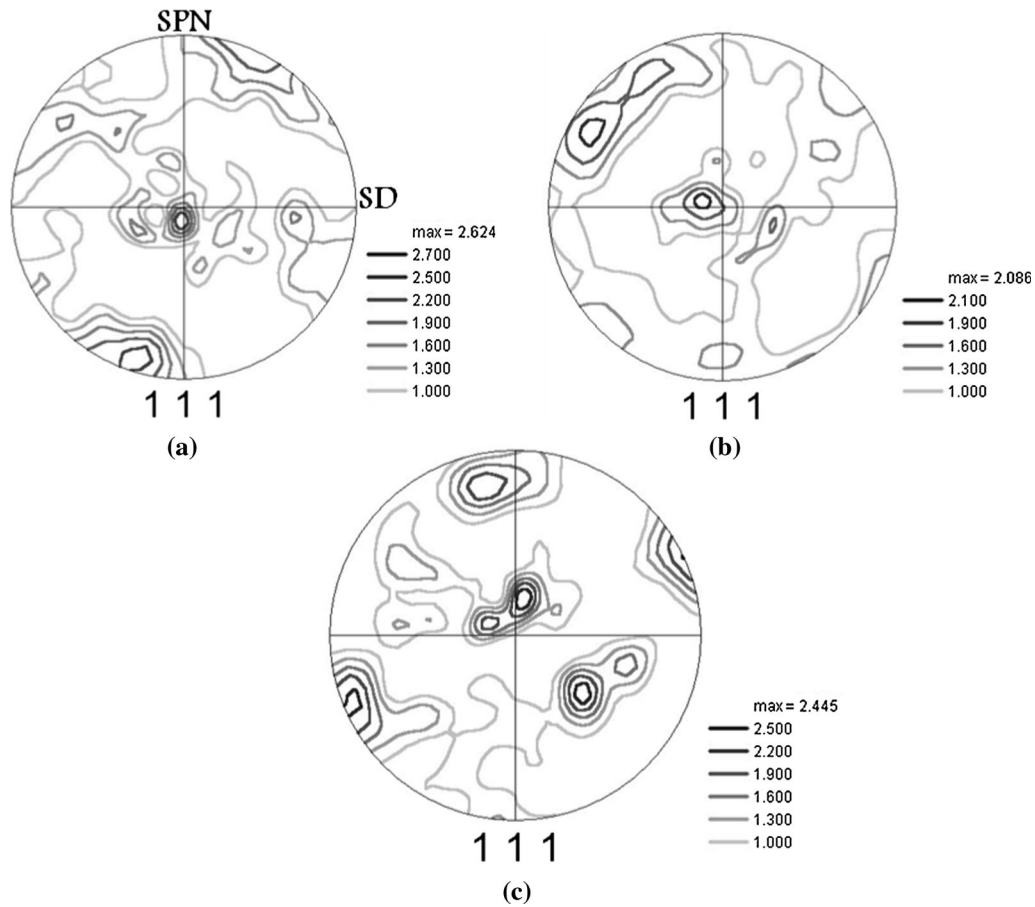

Fig. 6—111-pole figures representing micro-textures in the nugget zone of the alloy 2024 at (*a*) top, (*b*) middle, and (*c*) bottom. Frame of reference depicted in (a) is valid for all the pole figures.

Higher magnification EBSD scans from the nugget zone is shown in Figure 4 as grain boundary super-imposed IQ map, which depicts various stages of grain growth as per the two mechanisms mentioned. Low- and medium-angle grain boundaries are hardly visible in the middle of the nugget zone. In Figure 4(c), the region
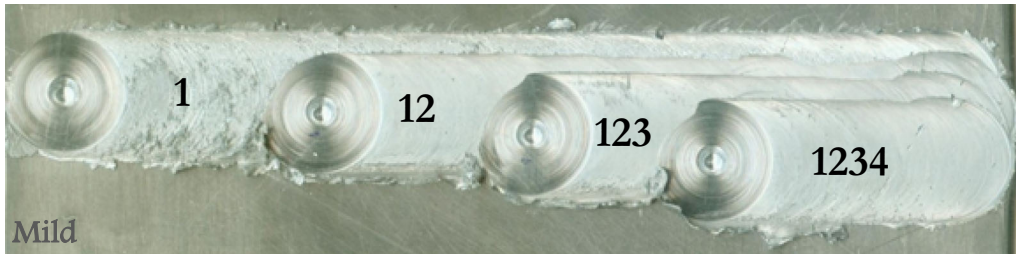
Fig. 7—Multiple-pass FSP specimens prepared on the alloy 2024 after four passes (*a*) MP-FSP corresponding to severe condition of strain and temperature with the specimen numbering system (*b*) MT-FSP corresponding to the mild condition of strain and temperature.
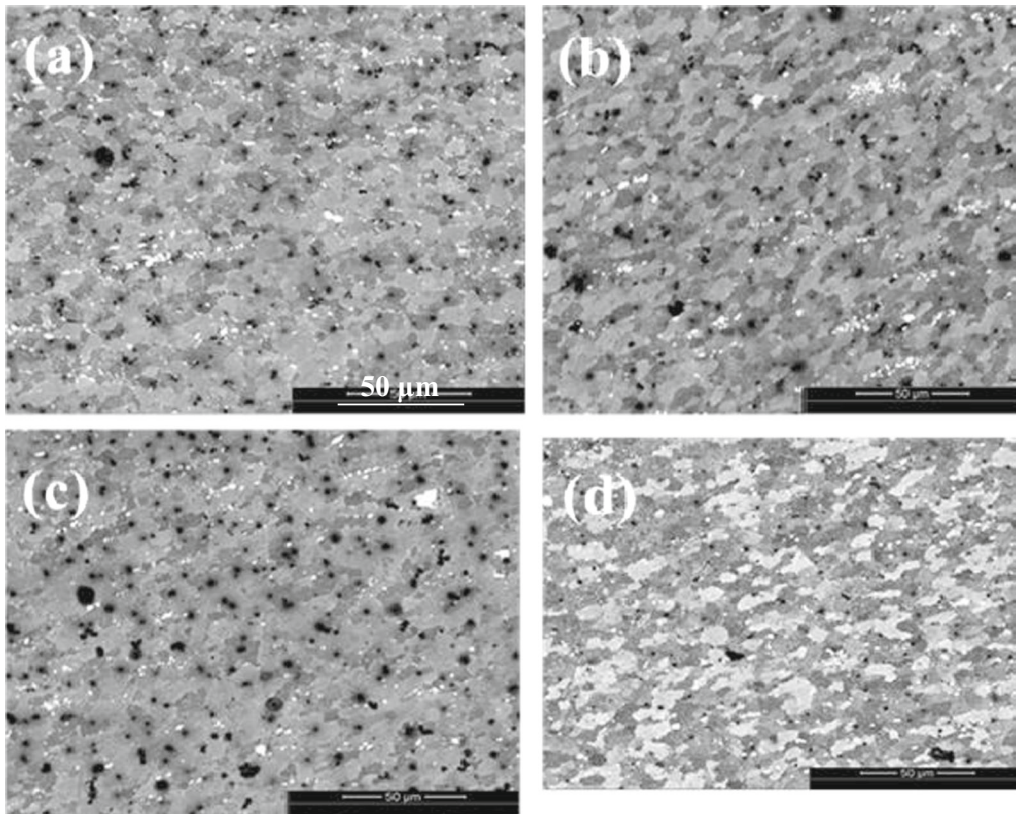

Fig. 8—Back-scattered electron micrograph representing the nugget zone after MP-FSP (*a*) first pass, (*b*) second pass, (*c*) third pass, and (*d*) fourth pass; enlarged scale bar as shown in (a) is applicable for all the images.

marked as A corresponds to the initiation of grain growth, which is surrounded by medium-angle grain boundaries. The resulting microstructure can be observed in Figure 4(d), and is marked as A, which is surrounded by high-angle grain boundaries. In both the cases, the boundary between the two arrowheads is connected by two grain boundary triple junctions. Region B marked in Figure 4(d) satisfies the conditions
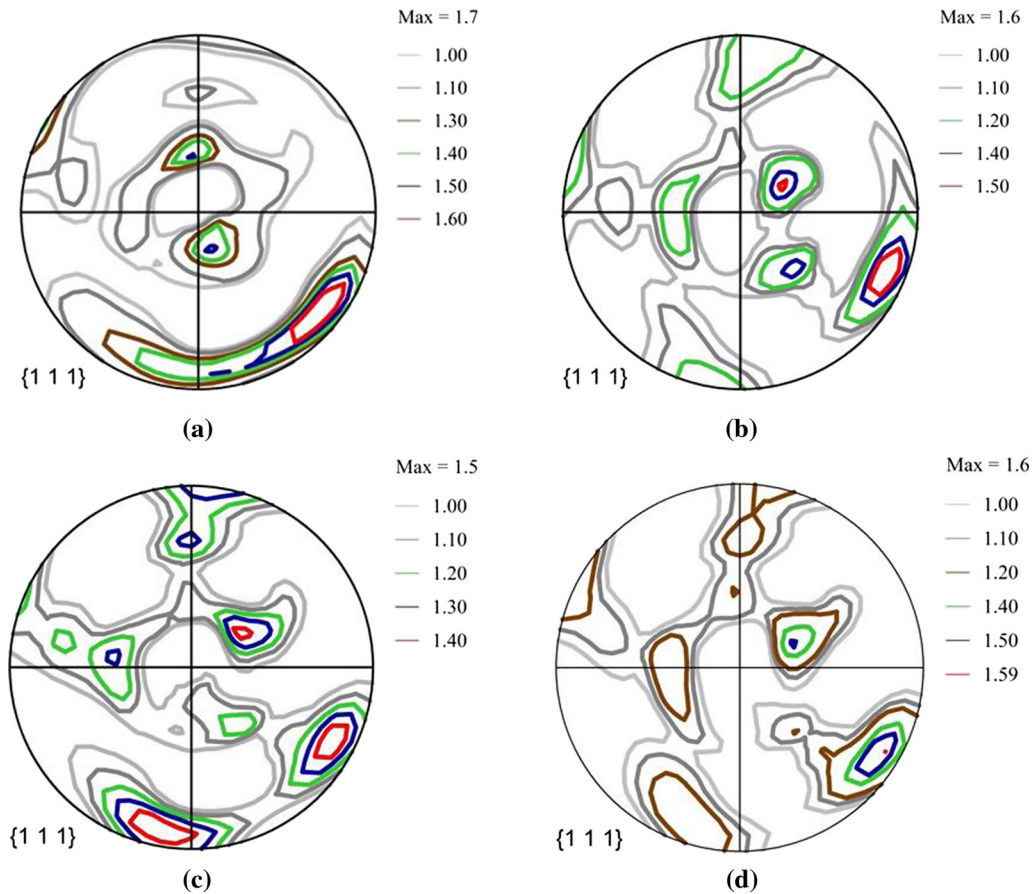
Fig. 9—111-pole figure corresponding to MP-FSP after (*a*) first pass, (*b*) second pass, (*c*) third pass, and (*d*) fourth pass. Frame of reference is same as depicted in Fig. 5(a) for all images.

for geometrical coalescence to occur. The boundary between the arrowheads is a medium-angle boundary, and the grains on either side are fully surrounded by high-angle grain boundaries.

Microstructural analysis carried out for the fully evolved microstructure in the nugget zone after FSP is indicative of DRX phenomenon with the abundance of strain-free grains. The phenomenon of DRX has been conceived as separate nucleation and grain growth stages in the preceding section, indicating the occurrence of discontinuous dynamic recrystallization (DDRX). Owing to high stacking fault energy (SFE) of aluminum, DRV is a dominant mechanism,[32] and hence, the possibility of discontinuous dynamic recrystallization (DDRX) is excluded in many of the previous studies.[33,34] Nugget zone microstructure after FSP depicts many large particles that are sufficient to act as nuclei for PSN mechanism to be operative. It has been reported earlier that the large second phase particles can enhance recrystallization.[35] As these particles grow, the coherency with the matrix is lost and the deformation field surrounding these particles can act as nuclei for DRX. This is observed as many bulges in the NZ microstructure (Figure 4). If the rate of particle coarsening is higher than the rate at which DRV takes place, then DRX can occur in the material as separate

nucleation and grain growth stage when the deformation proceeds. The high temperatures and large strain rates, together with the moderate cooling rates observed during FSP, can further enhance DDRX. As the processed material cools down dissolution and re-precipitation of particles can occur, leading to inhibition of grain growth, and an equi-axed microstructure is observed in the nugget zone. The grain boundary migration rates are low in Continuous Dynamic Recrystallization (CDRX). However, in FSP, the high shear stresses and the high temperatures can enhance the boundary movements. This further validates the occurrence of DDRX during FSP of the alloy 2024.

Deformation mode in FSP is considered as simple shear,[36] and hence, texture of the processed materials is usually expressed in the frame of reference for shear deformation as described in References 37 through 40. The reference co-ordinate system is such that shear direction (SD) and shear plane normal (SPN) are at 90 deg from the centre of the pole figure. Important components of the shear texture[38] are listed in the Table III. Bulk texture in the optimally processed sample is shown in Figure 5, and it is noteworthy that the texture further weakens after FSP. The texture components are shifted slightly and rotated away from their ideal positions in PF and ODF.
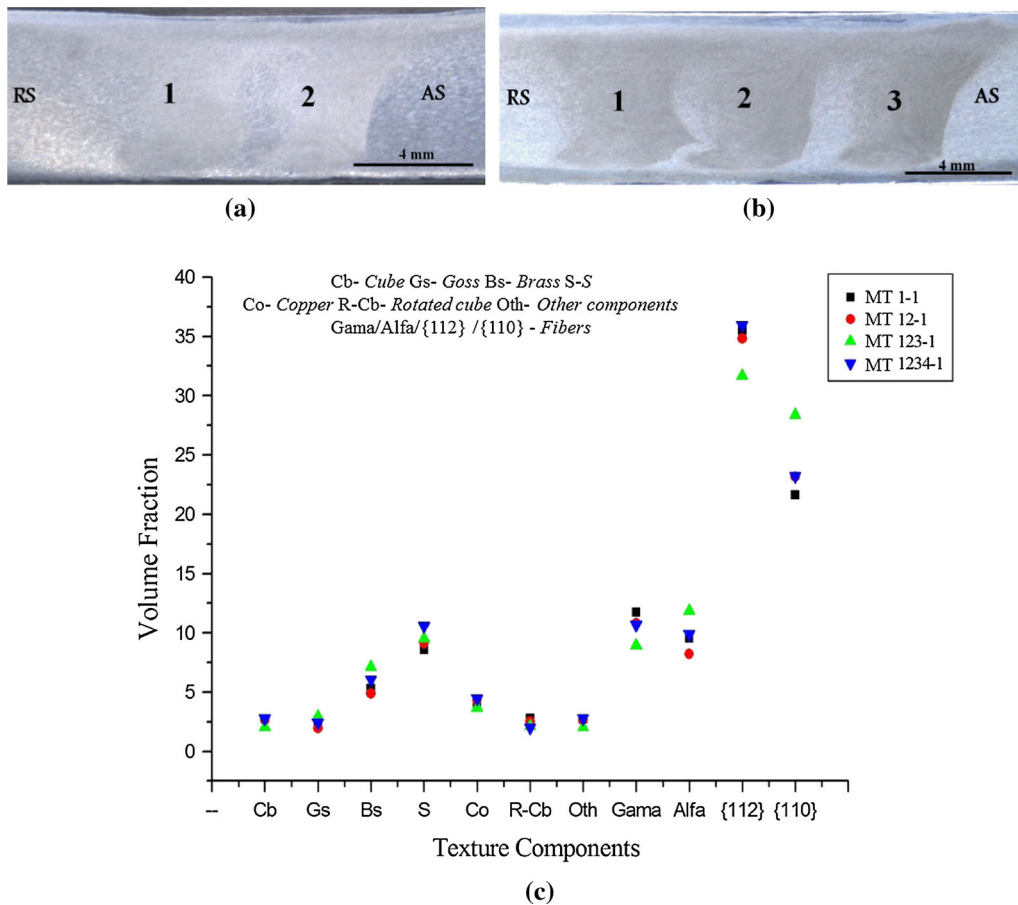
(a)

(b)

(c)

Fig. 10—Transverse cross-section macrograph corresponding to the MT- FSP carried out in the alloy 2024 with the nugget zone of respective passes mentioned (*a*) after two passes (*b*) after three passes; (*c*) volume fraction of texture components observed in the nugget zone of the first pass after successive passes.

Major component of texture observed from the pole figure and ODF are the fibers containing C and A_2^* components. Relatively lower intensities are observed at the locations of $A/\bar{A}$ and $B/\bar{B}$ components in the ODF sections. The general trend of texture development indicates a weakening of texture with the shear components retained. A correlation could be made between bulk texture and the micro-texture of different regions across the thickness at top, middle and bottom of the nugget zone. Pole figures in Figure 6 reveal variations in the strength of texture components at different regions in the nugget zone. Similar heterogeneities in the crystallographic texture was also observed in the nugget zone of aluminum alloys by Sato *et al.*[41] and Field *et al.*[42] The C component of the shear texture is quite prominent in the top and middle of the nugget zone. In FSP, frictional heating is maximum at the top surface of the work piece where the effect of tool shoulder is predominant. This effect of the compressive action by the tool shoulder is similar as that observed in rolling (excluding the effect of a tool pin), and higher temperatures are developed at the top of nugget zone. Hence, the development of a C component in the top of the nugget zone could be an effect of intense shear deformation. The relatively finer grains in the bottom have increased the randomness of texture, whereas bulk texture is a direct indication of the micro-texture observed in the top and middle. Similar weak textures are reported in pure aluminum by Montheillet *et al.*[38] For the alloy 2024 considered in this study, this effect is further enhanced due to PSN. It is well known that PSN as a DRX mechanism can weaken the crystallographic texture development in aluminum alloys and other materials.[28]

In the middle of the nugget zone, the C component is retained along with the development of $B/\bar{B}$ orientations, whereas in the bottom of nugget zone, textures observed are entirely different with the dominance of $B/\bar{B}$ components. Texture components in the top, middle, and bottom of the nugget zone are shifted slightly from the respective ideal positions, probably due to the shape of the tapered tool pin geometry, which is used for FSP and the imposed deformation conditions. EBSD measurements also reveal weak texture which is consistent with the bulk textures measured using XRD. Texture evolution confirms the stability of shear texture components even at the high temperature as developed during FSP.
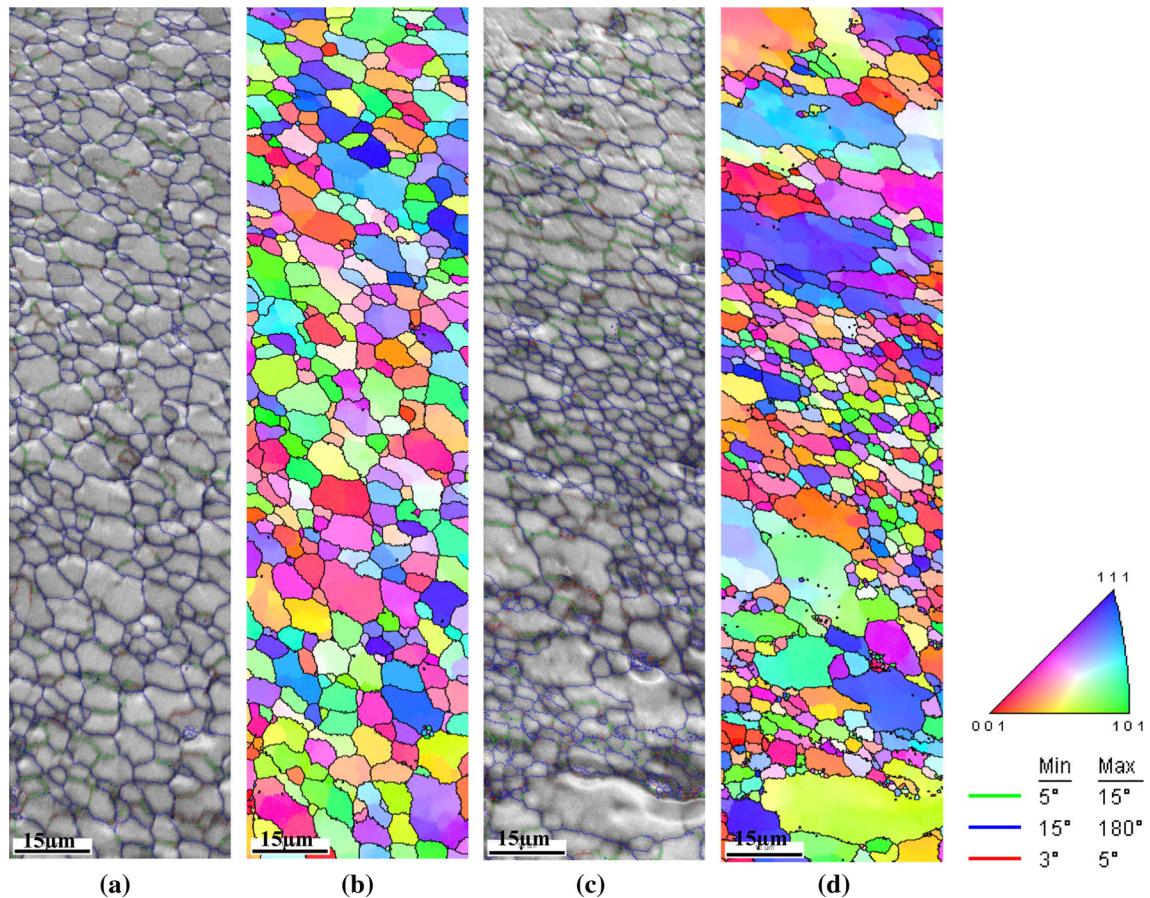
Fig. 11—IQ maps super-imposed with grain boundaries and corresponding IPF maps representing the nugget zone microstructure after heat treatment carried out at 723K (450 °C) for 30 min. (*a*) and (*b*) top of the nugget zone (*c*) and (*d*) bottom of the nugget zone.

B. *Microstructure and Texture Evolution During Multiple-Pass FSP*

The specimens prepared using the different multiple-pass processing (re-processing) strategies, MP-FSP and MT-FSP, are depicted in Figure 7. Moreover, it is noteworthy that the surface finish after the first pass (labeled as 1) is not smooth in either cases. However, a better finish was obtained from the second pass (labeled as 12) onwards. This trend is followed with the increase in number of passes. This indicates that the multiple-pass processing can be also employed to improve the surface finish after FSW/FSP of aluminum alloys. Microstructural evolution with the number of passes during MP-FSP, as obtained from SEM, is shown in Figure 8. Micrographs were taken at a similar magnification, and it can be observed that the gross microstructural features including the average grain size remains the same in all the four passes. Black dots on each micrograph are the reaction products after electro-polishing of the specimens.

Bulk texture evolution during the MP-FSP is shown in Figure 9 as a 111-pole figure. The evolution of texture is almost complete after the first pass, as it is evident from the figure. As the number of passes increase, pole figures reveal identical components of texture, and the total intensity of texture decreases slightly. The shear texture components retain their ideal orientation even with the temperatures generated being as high as 673 K to 823 K (400 °C to 550 °C) during FSP. Texture evolution during multi-pass FSP is almost like the texture observed in the optimally processed sample.

In the present study, multi-pass FSP was carried out to study the effect of mild (MT-FSP) and severe (MP-FSP) conditions of strain and temperature on the stability of microstructure and crystallographic texture developed during processing. Microstructural stability in the nugget zone was earlier reported for the multi-pass FSW of aluminum alloy 7050.[43] A similar work on multi-track FSP was carried out on the strain hardenable alloy 5086-O.[44] The specific processing route followed without allowing any gap between the successive passes confirmed stability of the microstructures. Findings from the present study corroborate with the results of these previous studies.

The macroscopic view of the transverse section representing multiple-pass FSP carried out using the MT-FSP route is shown in Figures 10(a) and (b). Nugget zone of the respective passes are depicted using the numbers in the respective images. As mentioned in the experimental section, MT-FSP with the successive
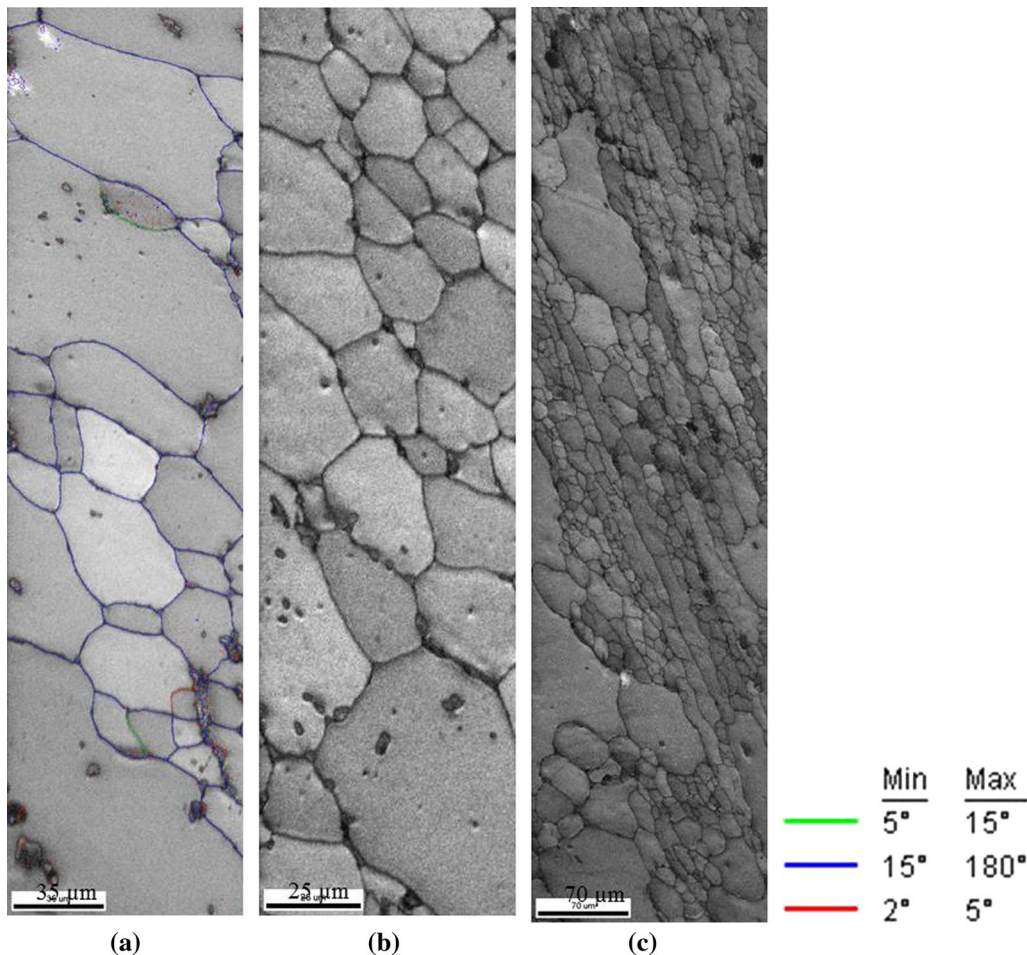
Fig. 12—Processed zone microstructure after heat treatment at 823 K (550 °C) for 30 min. (*a*) IQ map super-imposed with grain boundaries representing the top of NZ; IQ maps representing (*b*) middle of the NZ and (*c*) TMAZ on advancing side.

passes in lower processing distances will allow the possibility to track the nugget zone of first pass. Microstructure observed in the nugget zone of the first pass remained the same as in MP-FSP (Figure 8), while the heat and strain input are always lesser in MT-FSP. However, the texture development during MT-FSP could be of significant interest and the same is given in Figure 10(c) as a plot of volume fraction against the texture components. It is to be noted that the last four fiber texture components in the X-axis will also include some of the other components given earlier, and hence their larger volume fraction is accounted. Volume fraction of the minor components of texture remained almost the same after successive passes. Slight differences are observed in the volume fraction of the fiber texture components observed after the third pass in comparison to the other passes. This difference could be attributed to the contribution from a relatively wider boundary region separating the nugget zone of second and third pass as depicted in Figure 10(b). However, these variations are less significant (~ 35 *vs* 32 pct for {112} and 22 *vs* 27 pct for {110} fibers) to have a further detailed discussion about the same.

Another important point to be noted is that the initial temper and starting microstructure do not have

noticeable effect on the microstructure and texture of the nugget zone after FSP. Both microstructure as well as texture, are quite pronounced in the first pass and further passes, leading to identical microstructures and textures. Bulk texture measurements reveal weaker textures and the positions of maximum intensity in the orientation space remain the same during multiple-pass FSP. Only a slight shift of texture components is observed in the successive passes with respect to the optimally processed (single-pass FSP) sample. Similar textures obtained after single pass and multiple passes indicate the stability of microstructure and texture. This corroborates the earlier finding[45] that the initial microstructural state of the material does not have any effect on the microstructure and texture development during FSP. No grain growth seems to have occurred during multiple passes of FSP, even though significantly higher temperatures are involved in each of the successive passes. The higher temperatures may be lowering the strain energy, owing to the recovery process, thus reducing the accumulated strain level, which does not allow microstructural changes to occur. Dominant texture components are the ones that retain their stable orientation even with the temperatures generated being as high as 673 K to 823 K (400 °C to 550 °C) in
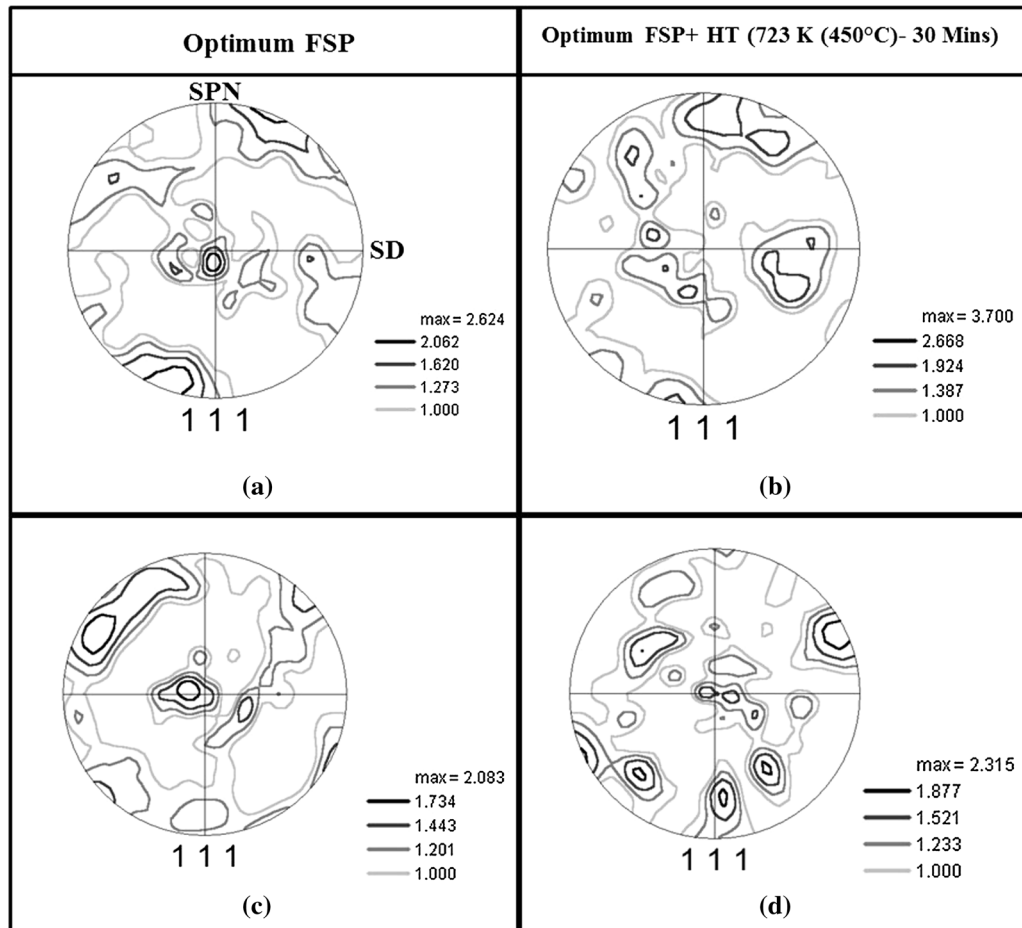
	Optimum FSP	Optimum FSP+ HT (723 K (450°C)- 30 Mins)

Fig. 13—Comparison of micro-texture in the top and middle of the nugget zone of the optimally processed sample of the alloy 2024 (*a, c*) and post-FSP heat-treated [723 K (450 °C)] sample (*b, d*). Frame of reference depicted in (a) is applicable to all the pole figures.

FSP. The *C* component is predominant in all the passes with minor contributions from the other shear texture components. Texture evolved during multiple-pass FSP is the same as that observed in the optimally processed sample subjected to a single-pass FSP.

C. *Effect of a Post-FSP Heat Treatment*

The grain boundary super-imposed IQ map and the IPF map for the optimum FSP sample that was heat treated at 723 K (450 °C) for 30 minutes is shown in Figure 11. It can be noted that grain growth has not occurred at the top (Figure 11(a)) of the nugget zone, rather the microstructure was recovered into a strain-free structure. But in the bottom of the nugget zone (Figure 11(c)), a few larger grains are observed, indicating the occurrence of grain growth.

Microstructural features after heat treatment carried out at 823 K (550 °C) is shown in Figure 12(a) through (c)). Significant grain growth has occurred in the nugget zone with the average grain size reaching about 30 μm (Figure 12(b)). A fully recovered strain-free structure is observed in all the micrographs. In the advancing side, shown in Figure 12(c), the deformed grains in the TMAZ are still retained but recovered.

IQ maps corresponding to the sample heat treated at 723 K (450 °C) revealed that grain growth occurred at the bottom of the nugget zone and not at the top or in the middle. Relatively smaller grains were observed in the bottom of nugget zone after FSP, and hence the energy associated with the grain boundaries was recorded to be high. Grain growth can easily occur in such favorable situations. The other reason for the observed grain growth can be attributed to the banded microstructure observed in the bottom region of the nugget zone. This structure is characterized by very high misorientations within some of the grains. Consequently, due to the associated higher strain energy, it can undergo recovery during the post-processing heat treatment. The recovery processes can be further aided by geometric coalescence in a condition when the neighbouring grains of similar orientations meet.[46] For a similar alloy, a post-welding heat treatment at 723 K (450 °C) for 2 hours resulted in a stable fine equi-axed grain structure in the nugget zone.[47] The large precipitates of Al₂CuMg shown earlier (Figure 3) are stable up to this temperature,[28] and hence can pin the grain boundaries and hinder the grain growth.

For a comparison, the average grain size in the nugget zone of the optimum FSP sample and that of the sample

Table IV. Comparison of the Average Grain Size at Various Regions in the Nugget Zone of the Optimally Processed and Heat-Treated (723 K (450 °C) for 30 min) Sample of the Alloy 2024

Location	Type of Specimen and Average Grain Size in μm	
	Optimal FSP	Optimal FSP + Heat Treated [723 K (450 °C)-30 min]
Top	7.5	6.5
Middle	6.2	4.6
Bottom	7.5	9.3

heat treated at 723 K (450 °C) for 30 minutes is given in Table IV.

It could be noticed that the grain size in the top and middle of the nugget zone is lower for the heat-treated sample than the optimally processed FSP sample. This is in accordance with the general understanding of grain growth at higher temperatures. The small decrease in grain size after heat treatment is also considered. Nucleation can easily occur at deformation bands in the processed zone microstructure due to the higher strain energy associated within them. Grain growth followed by nucleation could lead to the development of finer grains in the absence of pinning precipitates, and hence, the observed reduction in grain size can be accounted for. At the bottom, grain growth occurs and leads to an increase in the average grain size compared to the optimum FSP sample. With the variation in grain size observed in different regions, the total average grain size including top, middle, and bottom regions of the nugget zone remain the same in the optimally processed and the heat-treated specimens after FSP.

For the heat treatment carried out at 823 K (550 °C), if the temperature is significantly higher and above the solutionizing temperature for the alloy, the dissolution of particles will occur. Due to the presence of equi-axed grains surrounded by high-angle grain boundaries, as in the nugget zone microstructure, the time needed for grain growth is expected to be lesser than that in a cold worked material. High temperatures during deformation can result only at very low strain energy in the nugget zone microstructure after FSP than in the microstructures obtained by SPD techniques.[48] The dominance of recovery processes in aluminum alloys, even at temperatures as high as 823 K (550 °C), could be observed in the microstructure for the advancing side after the heat treatment (Figure 12(c)). The TMAZ in the advancing side retains the sheared layers of deformed grains at this temperature along with the associated recovery processes.

The micro-texture observed in the top and middle of the nugget zone of the optimally processed samples and two heat-treated samples are compared, and are shown in Figure 13. It can be observed that the shear components of texture are stable up to 723 K (450 °C). At 823 K (550 °C), grain growth occurs, and there were not sufficient grains observed to develop a reliable texture.

IV. CONCLUSIONS

Microstructure and texture evolution in the aluminum alloy 2024 was investigated after single-pass FSP and two different multiple-pass FSP strategies. Based on the results obtained after the characterization and analysis, the following conclusions can be drawn:

1. Equi-axed microstructure evolves in the nugget zone with an average grain size of 4-5 μm and a high fraction of HAGB's. DRX is the dominant restoration mechanism in the nugget zone with PSN as participating nucleation mechanism. Burke and Turnbull mechanism and geometric coalescence were observed as the mechanisms of grain growth.
2. Gradients in texture are observed across the thickness with shear texture components as the dominant components. The C component is dominant at the top of nugget zone indicating high temperature-high strain deformation. The dominance of deformation texture components depicts dynamic restoration mechanisms in the alloy during FSP. A weaker bulk texture, in agreement with the varied micro-texture across the thickness, could be attributed to the PSN mechanism and the continuous change in shear directions during FSP.
3. Stable microstructure and texture were observed after the different multiple-pass processing routes employed, -MP-FSP and MT-FSP-, which induced extreme and mild combinations of strain and temperature, respectively. This is ascribed to the high-temperature tortuous deformation path followed during the process that induces similar strain in the successive passes, leading to recovery in each pass.
4. Post-processing heat treatment indicates stability of microstructures up to temperatures as high as 723 K (450 °C). This could be attributed to the high temperatures involved in FSP, which retains lower strain energies in the processed materials.

REFERENCES

1. E.A. Starke, Jr and J.T. Staley: *Progr. Aerosp. Sci.*, 1996, vol. 32, pp. 131–72.
2. J.C. Williams and E.A. Starke: *Acta Mater.*, 2003, vol. 51, pp. 5775–99.
3. F. Tariq, N. Naz, and R.A. Baloch: *J. Non-destr. Eval.*, 2012, vol. 31 (1), pp. 17–33.
4. R.Z. Valiev, A.V. Korznikov, and R.R. Mulyukov: *Mater. Sci. Eng. A*, 1993, vol. 168 (2), pp. 141–48.
5. A. Azushima, R. Kopp, A. Korhonen, D.Y. Yang, F. Micari, G.D. Lahoti, and P. Groche: *CIRP Ann. Manuf. Technol.*, 2008, vol. 57 (2), pp. 716–35.
6. A. Krishnaiah, U. Chakkingal, and P. Venugopal: *Scr. Mater.*, 2005, vol. 52 (12), pp. 1229–33.
7. T.G. Langdon: *Acta Mater.*, 2013, vol. 61 (19), pp. 7035–59.
8. S. Biswas, S.S. Dhinwal, and S. Suwas: *Acta Mater.*, 2010, vol. 58 (9), pp. 3247–61.
9. P. Venkatachalam, S. Roy, V. T. Paul, M. Vijayalakshmi, B. Ravisankar, S. Suwas: *Materials Science Forum*, Vols. 702–703, pp. 113–18.
10. L.S. Tóth, R.A. Massion, L. Germain, S.C. Baik, and S. Suwas: *Acta Mater.*, 2004, vol. 52 (7), pp. 1885–98.
11. T. Mungole, N. Nadammal, K. Dawra, P. Kumar, M. Kawasaki, and T.G. Langdon: *J. Mater. Sci.*, 2013, vol. 48 (13), pp. 4671–80.
12. T. Mungole, P. Kumar, M. Kawasaki, and T.G. Langdon: *J. Mater. Res.*, 2014, vol. 29, pp. 2534–46.
13. W. Skrotzki, N. Scheerbaum, C. G. Oertel, H.G. Brokmeier, S. Suwas, and L.S. Tóth: Materials Science Forum, 2006, Trans Tech Publications, vol. 503, pp. 99–106.
14. S. Roy, B.R. Nataraj, S. Suwas, S. Kumar, and K. Chattopadhyay: *J. Mater. Sci.*, 2012, vol. 47 (17), pp. 6402–19.
15. K.S. Suresh, S. Sinha, A. Chaudhary, and S. Suwas: *Mater. Charact.*, 2012, vol. 70, pp. 74–82.
16. R.S. Mishra, M.W. Mahoney, S.X. McFadden, N.A. Mara, and A.K. Mukherjee: *Scr. Mater.*, 2000, vol. 42, pp. 163–68.
17. N. Nadammal, S.V. Kailas, and S. Suwas: *Mater. Des.*, 2015, vol. 65, pp. 127–38.
18. M.A. Sutton, B. Yang, A.P. Reynolds, and R. Taylor: *Mater. Sci. Eng. A*, 2002, vol. 323 (1), pp. 160–66.
19. I. Charit and R.S. Mishra: *Mater. Sci. Eng. A*, 2003, vol. 359 (1), pp. 290–296.
20. H. Aydin, A. Bayram, A. Uguz, and K.S. Akay: *Mater. Des.*, 2009, vol. 30 (6), pp. 2211–21.
21. J.Q. Su, T.W. Nelson, and C.J. Sterling: *Scr. Mater.*, 2005, vol. 52 (2), pp. 135–40.
22. R.W. Fonda, K.E. Knipling, and D.J. Rowenhorst: *JOM*, 2014, vol. 66 (1), pp. 149–55.
23. James C. M Li (ed.): *Mechanical Properties of Nanocrystalline Materials*, 2011, CRC Press: Boca Raton, p. 140.
24. A. Arora, Z. Zhang, A. De, and T. DebRoy: *Scr. Mater.*, 2009, vol. 61 (9), pp. 863–66.
25. Z. Hu, S. Yuan, X. Wang, G. Liu, and Y. Huang: *Mater. Des.*, 2011, vol. 32 (10), pp. 5055–60.
26. W. Xu, J. Liu, G. Luan, and C. Dong: *Mater. Des.*, 2009, vol. 30 (6), pp. 1886–93.
27. K. Oh-ishi, A.P. Zhilyaev, and T.R. McNelley: *Metall. Mater. Trans. A*, 2005, vol. 37A, pp. 2239–51.
28. A. Rollett, F.J. Humphreys, G.S. Rohrer, M. Hatherly: *Recrystallization and Related Annealing Phenomena*, Elsevier, 2004.
29. J.E. Burke and D. Turnbull: *Progr. Mater. Phys.*, 1952, vol. 3, pp. 220–92.
30. J.P. Nielsen: *ASM Seminar Series*, American Society for Metals, Metals Park, Ohio, 1966.
31. N. Nadammal, S.V. Kailas, J.A. Szpunar, and S. Suwas: *Metall. Mater. Trans. A*, 2015, vol. 46A, pp. 2823–28.
32. H.J. McQueen and W. Blum: *Mater. Sci. Eng. A*, 2000, vol. 290, pp. 95–107.
33. H.J. McQueen: *Mater. Sci. Eng. A*, 2004, vols. 387–389, pp. 203–08.
34. S. Gourdet and F. Montheillet: *Acta Mater.*, 2003, vol. 51, pp. 2685–99.
35. F.J. Humphreys: *Acta Metall.*, 1977, vol. 25 (11), pp. 1323–44.
36. R.W. Fonda, J.F. Bingert, and K.J. Colligan: *Scr. Mater.*, 2004, vol. 51, pp. 243–48.
37. F. Montheillet, M. Cohen, and J.J. Jonas: *Acta Metall.*, 1984, vol. 32 (11), pp. 2077–89.
38. F. Montheillet, P. Gilormini, and J.J. Jonas: *Acta Metall.*, 1985, vol. 33 (4), pp. 705–17.
39. G.R. Canova, U.F. Kocks, and J.J. Jonas: *Acta Metall.*, 1984, vol. 32 (2), pp. 211–26.
40. W. Cai, J. Mabon, and P. Bellon: *Wear*, 2009, vol. 267, pp. 485–94.
41. Y.S. Sato, H. Kokawa, K. Ikeda, M. Enomoto, T. Hashimoto, and S. Jogan: *Metall. Mater. Trans. A*, 2001, vol. 32 (4), pp. 941–48.
42. D.P. Field, T.W. Nelson, Y. Hovanski, and K.V. Jata: *Metall. Mater. Trans. A*, 2001, vol. 32A (11), pp. 2869–77.
43. R. Brown, W. Tang, and A.P. Reynolds: *Mater. Sci. Eng. A*, 2009, vol. 513, pp. 115–21.
44. K.N. Ramesh, S. Pradeep, and V. Pancholi: *Metall .Mater. Trans. A*, 2012, vol. 43A, pp. 4311–19.
45. V. Dixit, R.S. Mishra, R.J. Lederich, and R. Talwar: *Sci. Technol. Weld. Join.*, 2007, vol. 12 (4), pp. 334–40.
46. R.E. Reed-Hill: *Physical Metallurgy Principles*, 2nd ed., D. Van Nostrand Company, New York, 1973, pp. 302–03.
47. H. Aydin, A. Bayram, and I. Durgun: *Mater. Des.*, 2010, vol. 31, pp. 2568–77.
48. J. Gubicza, S.V. Dobatkin, E. Khosravi, A.A. Kuznetsov, and J.L. Lábár: *Mater. Sci. Eng. A*, 2011, vol. 528 (3), pp. 1828–32.